JOURNAL OF AIRCRAFT
Vol. 48, No. 3, May–June 2011

Aerodynamic Effects of Structural Flexibility in Two-Dimensional Insect Flapping Flight

Kuen-Bae Lee,* Jin-Ho Kim,† and Chongam Kim‡
Seoul National University, Seoul 151-742, Republic of Korea

DOI: 10.2514/1.C031115

Interaction between a flexible flapping wing and the ambient fluid is of considerable importance in realistic flapping flight. In this paper, two-dimensional fluid–structure interaction simulations are conducted to examine realistic flow features of insects' flapping motion and to investigate aerodynamic change due to structural flexibility of insect wings under a forward-flight condition. Three types of airfoils are considered to reflect structural deformation. Compared with earlier studies regarding two-dimensional rigid-airfoil simulations, the same key physical phenomena and flow patterns could be observed in the flexible case. For example, lift is mainly generated during downstroke by effective angle of attack and leading-edge vortex, while a large amount of thrust is impulsively generated at the end of upstroke by vortex pairing and vortex staying. On the other hand, the quantitative aspect of flowfields is somewhat different. Structural deformation does affect aerodynamic force generation pattern, and thus structural flexibility has a significant impact on aerodynamic performance. Aerodynamic force coefficient and propulsive efficiency are enhanced compared with the case of a rigid airfoil. In addition, numerical simulations are performed to inspect effects of aerodynamic parameters such as the Reynolds number and reduced frequency. From extensive numerical comparisons, it is observed that key physical phenomena such as vortex pairing and vortex staying are still observed in other flow conditions.

Nomenclature

$[C]$	=	damping matrix
C_d	=	drag coefficient
C_l	=	lift coefficient
C_t	=	thrust coefficient (negative drag coefficient)
c	=	chord length
c_i	=	instantaneous aerodynamic coefficient
E	=	modulus of elasticity
e_c	=	a number of subelements
e_i	=	area coefficient
$\{F\}$	=	external aerodynamic load
f	=	flapping frequency, Hz
h_a	=	dimensionless plunging amplitude
J	=	Jacobian of transformation matrix
$[K]$	=	stiffness matrix
k	=	reduced frequency, $(fc/U_{\max})$
$[M]$	=	mass matrix
N_s^j	=	shape function
p	=	pressure
Q	=	flow variable vector
$\hat{R}$	=	residual vector including inviscid and viscous fluxes
Re	=	Reynolds number $(U_{\max}c/\nu)$
R_s^j	=	force vector on solid mesh
S	=	area of the Delaunay graph
$\hat{S}$	=	unsteady sourcelike term
Str	=	Strouhal number (fc/U_0)
t	=	nondimensional time
$\tilde{t}_f$	=	force vector on fluid mesh
$\{U\}$	=	nodal displacement
$U_{\max}$	=	maximum relative velocity
U_0	=	freestream velocity
υ	=	freestream kinematic viscosity
$\mathbf{v}_a$	=	convection velocity
$\mathbf{v}_r$	=	relative velocity to reflect structural deformation
$\mathbf{v}$	=	flow velocity $(\mathbf{v}_a + \mathbf{w} + \mathbf{v}_r)$
$\mathbf{w}$	=	mesh velocity to represent the figure-of-eight motion
$x(t)$	=	lagging motion (horizontal motion)
$y(t)$	=	translation motion (vertical motion)
$\alpha(t)$	=	pitch-angle motion
β	=	artificial-compressibility parameter
Γ	=	common-refinement boundary
η	=	propulsive efficiency
ν	=	Poisson ratio
ρ	=	density of material
σ	=	viscous stress tensor
τ	=	pseudotime

Received 24 May 2010; revision received 21 November 2010; accepted for publication 16 January 2011.

*Graduate Student, Ph.D. Candidate, Interdisciplinary Program in Computational Science and Technology. Student Member AIAA.

†Graduate Student, Ph.D. Candidate, Department of Aerospace Engineering. Student Member AIAA.

‡Professor, Department of Aerospace Engineering and Institute of Advanced Aerospace Technology; chongam@snu.ac.kr. Senior Member AIAA (Corresponding Author).

I. Introduction

INSECTS' flapping flight has been regarded as one of the most interesting and challenging research subjects in the field of unsteady aerodynamics because of its potential applicability to various novel propulsive devices or next-generation aerial vehicles. Many researchers have conducted experimental or numerical studies to discover the unsteady aerodynamic characteristics of insects' flapping flight. However, reliable unsteady flowfield data that can explain realistic flow features or key physical phenomena of insects' flapping flight are not sufficiently available. One of the reasons is that most studies did not include the effects of structural flexibility. Fluid–structure interaction (FSI) simulation of insect flight usually requires additional experimental or numerical techniques. Considerable attentions have been paid to rigid flapping motions. Anderson et al. [1] visualized the flowfield around an oscillating airfoil and measured aerodynamic performance by investigating the flow pattern characteristics. Tuncer and Platzer [2] made numerical flow visualization using a particle-tracing technique and studied the effects of unsteady vortices on a flapping airfoil. Wang [3] simulated a two-dimensional moving airfoil to observe that the optimum frequency for a heaving airfoil was correlated to the time scale of vortex shedding of an impulsively started airfoil. Lewin and Haj-Hariri [4] analyzed

two-dimensional airfoil flows under prescribed heaving motions to show that the maximum propulsive efficiency at a given Strouhal number occurs at a particular heaving frequency. Based on the physical understanding on the role of leading- and trailing-edge vortices, Lee et al. [5] designed an optimal flapping airfoil sustaining a high propulsive efficiency and a high thrust coefficient. Kaya and Tuncer [6] optimized the path of a flapping airfoil undergoing a combined nonsinusoidal pitching and plunging motion to achieve the maximum thrust and propulsive efficiency. In particular, two-dimensional simulations of the realistic figure-of-eight motion under a forward-flight condition by Lee et al. [7] showed that the thrust is impulsively generated at the end of upstroke through the mechanisms of vortex pairing and vortex staying. However, only a few studies have been attempted on realistic flexible flapping motion. Experimental studies on flexible flapping airfoils were carried out by Heathcote and Gursul [8]. They visualized flowfields around a chordwise flexible 2-D airfoil oscillating in heave at low Reynolds numbers and measured thrust and propulsive efficiency. In addition, they observed an optimal thickness of the airfoil and the plunging frequency that produced the highest thrust and propulsive efficiency. Aside from experimental studies, some researchers have conducted computational works around flexible flapping airfoils. Pederzani and Haj-Hariri [9] investigated the effect of chordwise flexibility on heaving airfoils using a FSI numerical model for 2-D unsteady viscous flows around a flexible body. They observed that the change of the flowfields by the flexible airfoil altered the forces acting on the airfoil in a way that the flexible airfoil was more efficient than the rigid one for different plunging frequency. Oliver et al. [10] carried out some test simulations using a vortex-excited elastic plate behind a bluff body and presented preliminary results on flexible flapping wings. Chandar and Damodaran [11] performed computational FSI simulations for predicting the deformation of a flapping wing due to aerodynamic forces. Shyy et al. [12] conducted numerical simulation to examine the flowfield around a flexible plunging airfoil under incoming flow and to observe the dynamic fluid characteristics and the mechanism of thrust generation. Effect of airfoil flexibility has been considered by coupling a finite element structural solver using beam elements with a fluid solver using the Navier–Stokes equations.

Previous studies have made meaningful progresses in understanding the unsteady flow characteristics of flexible flapping airfoils. However, further study is essential, especially in addressing the aerodynamic force generation caused by structural flexibility, which will definitely change local behaviors in thrust and propulsive efficiency. Furthermore, compared with studies of flexible airfoils under sinusoidal flapping motion (or combined pitching and heaving) [8–12], there are few results dealing with motions of flexible insect wings under realistic flight conditions such as forward flight and/or rapid maneuvering. In addition, accurate computations have to be carried out based on elaborate structural modeling and realistic shape of insect wing.

In the present work, detailed two-dimensional FSI simulations are conducted to investigate the realistic flow features of insects' flapping motion due to structural flexibility. A wing trajectory is chosen as a blowfly's wing motion, called the figure-of-eight motion, under a forward-flight condition. It is extracted from the results of Nachtigall's [13] tethered flight experiment.

In FSI simulations, there are two kinds of strategies to couple fluid and solid modules: the tightly coupling method and the loose coupling method [14,15]. In the first method, the fluid and solid modules are simultaneously marched by coupled systems of equations, and in the second method, the fluid and solid modules are independently marched before they exchange data necessary for boundary conditions. Drawbacks of the tightly coupling method are the ill-conditioned nature of the coupled system matrices and the rewriting of the fluid and solid modules, which seriously limit the applicability of the method. Consequently, the loose coupling method has been adopted in the present work. The unsteady incompressible Navier–Stokes equations with artificial-compressibility method are used as the fluid module [16], while the dynamic finite element equations using a direct time-integration method are employed as the solid module [17]. To exchange physical information to each module, the common-refinement method is employed as a data transfer method [18]. A simple but efficient dynamic grid deformation technique based on Delaunay graph mapping is used to deform computational grids [19].

The present paper is organized as follows. First, numerical methods and the modeling of flapping motion and airfoil (a sectional shape of 3-D insect wing) are introduced. Then some validation cases are presented to independently validate the fluid and solid modules as well as the FSI solver. After that, two-dimensional FSI simulations of the figure-of-eight motion are carried out in terms of stroke and motion component, and the computed results are compared in detail with the cases of a rigid airfoil. Finally, aerodynamic effects by changing nondimensional parameters such as Reynolds number and reduced frequency are examined.

II. Numerical Methods

A. Fluid Module

Because of the nature of low-Reynolds-number flows, the two-dimensional unsteady incompressible Navier–Stokes equations are employed as the governing equations:

$$\frac{\partial \mathbf{v}}{\partial t} + \mathbf{v} \cdot \nabla \mathbf{v} + \nabla p = \nabla \cdot \sigma \tag{1}$$

$$\nabla \cdot \mathbf{v} = 0 \tag{2}$$

where p denotes the pressure, $\mathbf{v} = \mathbf{v}_a + \mathbf{w} + \mathbf{v}_r$ is the flow velocity (where $\mathbf{v}_a$ is the convection velocity, $\mathbf{w}$ is the mesh velocity to represent the figure-of-eight motion, and $\mathbf{v}_r$ is the relative velocity to reflect structural deformation), and σ is the viscous stress tensor. Both pressure and stress tensor are normalized by the density. If the maximum relative velocity ($U_{\max}$), the chord length ($c = 3.8$ mm according to Nachtigall's experiment) and the inverse flapping frequency ($1/f$) are adopted as the characteristic velocity, length, and time scales, the Reynolds number and reduced frequency are defined as $Re = U_{\max} c/\nu$ and $k = fc/U_{\max}$. With these scaling parameters, the nondimensional form of the incompressible Navier–Stokes equations becomes

$$k\frac{\partial \mathbf{v}^*}{\partial t^*} + \mathbf{v}^* \cdot \nabla^* \mathbf{v}^* + \nabla^* p^* = \frac{1}{Re}\nabla^* \cdot \sigma^* \tag{3}$$

The artificial-compressibility method of Eq. (4) is then employed to iteratively update the velocity and pressure fields by satisfying the momentum equation, viz., Eq. (3):

$$\frac{\partial p}{\partial \tau} = -\beta \nabla \cdot \mathbf{v} \tag{4}$$

where β is the artificial-compressibility parameter. Throughout all computations, β is set to 200 for robust convergence.

Upwind-biased Osher's flux difference splitting is used for spatial discretization [16]. A third-order linear variable reconstruction is employed to attain a higher-order spatial accuracy. For time integration, the lower/upper symmetric Gauss–Seidel scheme is used together with the dual-time-stepping method. At each physical time step, a steady-state solution is obtained by the residual lower than $\mathcal{O}(10^{-5})$. The final discretized form of the governing equations can be expressed as

$$\left[\frac{I}{J\Delta\tau} + \left(\frac{\partial \hat{R}}{\partial Q} + \frac{\partial \hat{S}}{\partial Q}\right)^{n+1,m}\right]\Delta Q^{n+1,m} = -(\hat{R}^{n+1,m} + \hat{S}^{n+1,m}) \tag{5}$$

Here, the superscript n indicates the physical time level, m denotes the pseudotime iteration, $\hat{R}$ is the residual vector including the inviscid and viscous fluxes, $\hat{S}$ is an unsteady sourcelike term, Q is the flow variable vector, and J is the flux Jacobian. A detailed numerical implementation, including spatial discretization and time integration, can be found in [16].

Boundary conditions for the inflow and outflow regions are based on the method of characteristics and applied explicitly. The Jacobian matrix of the inviscid flux vector has at least one negative or one positive eigenvalue. At the inflow, there is one characteristic wave traveling out of the computational domain and two waves traveling into the domain. Thus, the velocity components are specified from the freestream conditions and the pressure is extrapolated from the interior points. At the outflow, two waves are traveling out of the domain and one is traveling into the domain. The pressure is specified and the velocity components are determined by extrapolation. Note that the velocity components are the approximation of the Riemann invariants corresponding to the characteristic waves [20]. On the solid wall, velocity is the same as the airfoil velocity to simulate time-dependent motions. Since the Reynolds number of interest is relatively low $[Re = \mathcal{O}(10^2) \sim \mathcal{O}(10^3)]$ all computations are conducted under the assumption of fully laminar flow. Standard parallel computing has been implemented through Message-Passing Interface programming to relieve computational overhead.

B. Structure Module

To obtain structural displacement in solid module, the dynamic finite element equations using a direct time-integration method are employed as the governing equations [17]:

$$[M]\{\ddot{U}\} + [C]\{\dot{U}\} + [K]\{U\} = \{F\} \tag{6}$$

In Eq. (6), $[M]$, $[C]$, and $[K]$ represent the mass matrix, damping matrix, and stiffness matrix, respectively; $\{U\}$ is the nodal displacement; and $\{F\}$ denotes the external aerodynamic load applied to each node.

The direct time-integration method is to obtain the response history using step-by-step temporal integration without changing the form of the dynamic finite element equations. The temporal response is thus evaluated by marching the time increment of Δt.

With the time step of Δt, velocity and acceleration at the nth time step are replaced by conventional central differencing approximation, as follows:

$$\{\dot{U}\}_n = \frac{1}{2\Delta t}(\{U\}_{n+1} - \{U\}_{n-1}) \tag{7}$$

$$\{\ddot{U}\}_n = \frac{1}{\Delta t^2}(\{U\}_{n+1} - 2\{U\}_n + \{U\}_{n-1}) \tag{8}$$

By inserting Eqs. (7) and (8) into Eq. (6), we have

$$\left(\frac{1}{\Delta t^2}[M] + \frac{1}{2\Delta t}[C]\right)\{U\}_{n+1} = \{F\}_n - [K]\{U\}_n + \frac{1}{\Delta t^2}[M](2\{U\}_n - \{U\}_{n-1}) + \frac{1}{2\Delta t}[C]\{U\}_{n-1} \tag{9}$$

The proper range of the allowable Δt is determined from the stability analysis, as follows:

$$\Delta t \le \frac{\Delta L}{\sqrt{E/\rho}} \tag{10}$$

where ΔL is the characteristic length of finite element, E is Young's modulus, and ρ is the density of material.

C. Data Transfer on Fluid–Solid Boundary and Dynamic Grid Deformation Technique

The fluid and solid modules are solved by the loose coupling method with different mesh densities. Along nonmatching fluid-solid interface, an interpolation technique is thus necessary to properly transfer the pressure and displacement into solid and fluid module, respectively.

A method based on the common-refinement is implemented as a data transfer technique between nonmatching meshes [18]. This method uses a so-called common refinement, which is composed of the intersection of the fluid and solid subelements along the common interface. First, the fluid interface nodes are projected onto the solid interface, where the normal vector at each fluid node is obtained by averaging the neighboring element normal vectors. Then the union of the original solid interface nodes and the projected nodes from the fluid interface are combined to create subelements on the solid interface. A similar inverse projection of the solid interface nodes onto the fluid interface is carried out to create the subelements on the fluid interface. The final subelements (or the common-refinement mesh) are then obtained from a convex combination of fluid and solid subelements. Along the common refinement, an integration of physical variables is carried out. For example, the load vector R_s^j over the common-refinement nodes can be computed as follows:

$$R_s^j = \sum_{i=1}^{e_c} \int_{\sigma_c^i} N_s^j \tilde{t}_f \, \mathrm{d}\Gamma \tag{11}$$

where R_s^j denotes the concentrated force vector at node j on the solid interface, N_s^j is the shape function associated with the node j, e_c indicates the number of subelements sharing the node j, σ_c^i denotes the ith subelement sharing the node j, $\tilde{t}_f$ is the force at fluid interface nodes, and Γ is the common interface boundary. A similar integration can be carried out to obtain displacement.

This method can accurately minimize the L_2 interpolation error, and it is conservative without producing numerical oscillations. Overall discretization error is $\mathcal{O}(h_f^2 + h_s^2)$, where h_f and h_s are the resolutions of the fluid and solid meshes, respectively. Further details can be found in [18].

Because of geometric deformation occurring at each time step, a dynamic grid deformation technique must be employed. A simple, efficient, and noniterative grid deformation technique based on the creation of a Delaunay graph of the original mesh is adopted in this work [19]. To create the triangular Delaunay graph, all of the geometric boundary points are connected to some reference points on the outer boundary (or outside) of computational domain. The area coefficients are then computed and stored as follows to locate the mesh points in the Delaunay graph after grid movement:

$$e_i = \frac{S_i}{S}, \qquad 1 \le i \le 3 \tag{12}$$

where S is the area of the Delaunay graph, and S_i is the area of subtriangles defined by the grid point i within the Delaunay graph. After moving the geometric boundary points according to a prescribed motion or structural deformation, a new set of coordinates is generated for the nodal points of the Delaunay graph. The mesh points within the Delaunay graph are then relocated such that the area coefficients of each mesh point are conserved after grid movement:

$$x'_P = \sum_{i=1}^{3} e_i x'_i, \qquad y'_P = \sum_{i=1}^{3} e_i y'_i \tag{13}$$

where (x'_P, y'_P) or (x'_i, y'_i) are the new coordinates of the mesh point and the nodal points of the Delaunay graph. Further details can be found in [19]. Figure 1 shows an example of the dynamic grid deformation for a flapping airfoil and histories of the cell aspect ratio distribution. It is seen that the cell aspect ratio of the original mesh is almost maintained, and the mesh quality is preserved during the dynamic grid deformation process.

D. Modeling of Motion Trajectory, Geometric Shape, and Structural Flexibility

It is difficult to precisely measure wing motion under complete free-flight conditions. A tethered flight experiment can be conducted as an alternative for tracking a wing trajectory, and it may properly mimic forward-flight conditions by superposing freestream velocity.

Several researchers have measured wing trajectories by using a wind tunnel and a high-speed camera system [13,21,22]. Nachtigall [13] suspended a blowfly in front of an open wind tunnel and adjusted

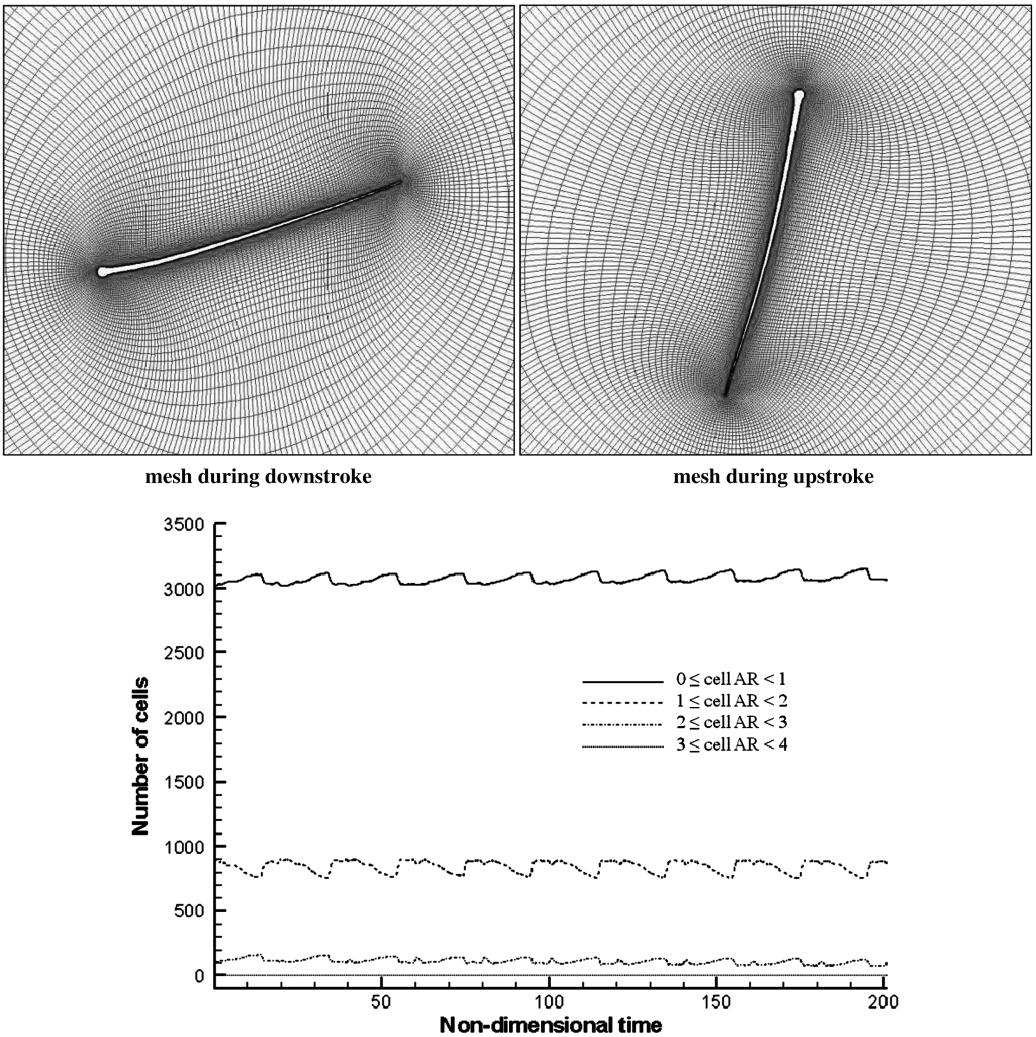

Fig. 1 Mesh deformation for a flapping airfoil (top) and histories of the cell aspect ratio distribution (bottom).

the wind speed until the net horizontal force acting on the blowfly was zero to realize forward-flight conditions. From a two-dimensional side view, the wing-tip trajectory of many insects resembles the figure eight, as shown in Fig. 2. The so-called figure-of-eight motion was first observed in 1869 by the French physiologist, Étienne-Jules Marey, as reported in [23]. Nachtigall's [13] experiment also exhibits the figure-of-eight motion of a blowfly wing whose trajectory can be expressed in terms of a Fourier series:

$$F(t) = a_0 + \sum_{n=1}^{m} a_n \cos(2n\pi kt) + b_n \sin(2n\pi kt) \qquad (14)$$

$$F(t) = [x(t), y(t), \alpha(t)]^T \qquad (15)$$

where a_0, a_n, and b_n are Fourier coefficients and k is the reduced frequency. The detailed coefficients can be found in [24]. Though the definition of the reduced frequency is similar to the Strouhal number ($Str = fc/U_0$), we use both to follow notational convention in two fields. In the literature of fluid mechanics, the Strouhal number is usually associated with the dimensionless shedding frequency, while the reduced frequency is popularly used in the literature of insect motion. Thus, we use the Strouhal number in validating the case of the airfoil oscillating with constant amplitude and the reduced frequency in flapping motion. Figure 2 shows the wing-tip trajectory obtained from Eq. (14). Freestream direction is the positive x direction, and thus lift and thrust are the positive y and negative x directions. Downstroke and upstroke motions are indicated by light and dark arrows, respectively. From the wing-tip trajectory measured at equal-time-interval, one can see that the interval between the wing positions is shorter during downstroke, indicating the wing motion during downstroke is relatively slow. The posture of the wing is almost horizontal, and the wing rotation is relatively mild. On the other hand, upstroke motion is fast and the leading edge is sharply pitched up. In particular, the rapid wing rotation is concentrated near the end of upstroke. In Fig. 2, the flapping-wing motion consists of

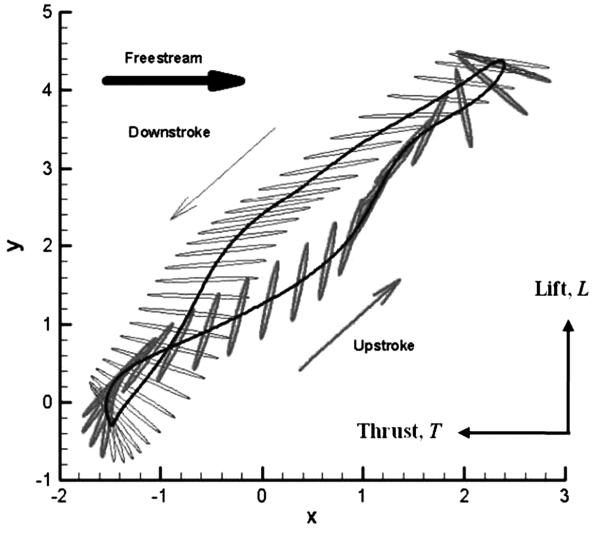

Fig. 2 Nondimensional position of a blowfly's wing element during tethered flight: downstroke phase and upstroke phase.

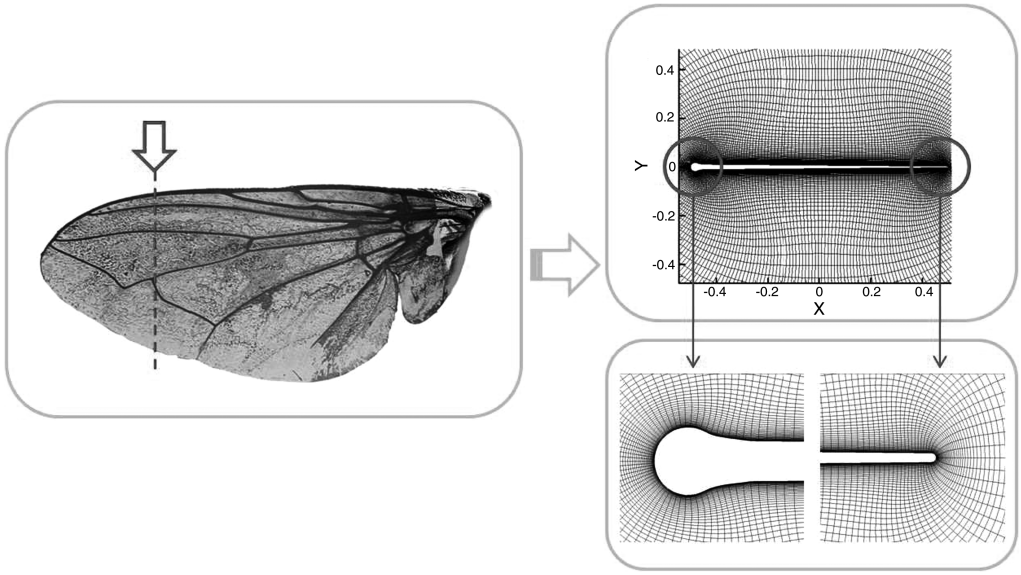

Fig. 3 Geometric modeling: a) real insect wing and b) tadpole-type wing.

three components: translation [$y(t)$: vertical motion], lagging [$x(t)$: horizontal motion], and rotation [$\alpha(t)$].

Because the vein system of a blowfly wing is complex, the precise cross-sectional shape (or airfoil shape) of the 3-D wing can be complicated (see Fig. 3a). For example, the thickness of vein is measured to be 3.63×10^{-2} mm and that of the trailing membrane is 1.2×10^{-2} mm [25]. By simplifying the geometric details while maintaining the main geometric characteristic, a tadpole type of airfoil can be obtained, as shown in Fig. 3. The airfoil thickness is linearly decreased from the leading edge after the vein to the trailing edge. The material properties are as follows: the modulus of elasticity E of vein and membrane is 6.1×10^9 N/m^2 and 1.5×10^9 N/m^2, respectively, and the density is 1200 kg/m^3 [26]. To investigate the flexibility effects of insect wing, three types of airfoils (rigid airfoil, linear type of flexible airfoil, and homogeneous type of flexible airfoil) are considered, as shown in Fig. 4. The infinity value of E indicates a rigid body and thus FSI simulation is not applied. The modulus of elasticity of the linear-type airfoil decreases linearly from 6.1×10^9 N/m^2 to 1.5×10^9 N/m^2 in the direction of the trailing edge, and that of the homogeneous type is the arithmetical mean of the two values. In both cases, 10% front part of airfoil is considered to be a rigid body because the stiffness in the vicinity of the leading edge is very high compared with other regions.

III. Code Validation

A. Validation of Baseline Solvers

As a validation case of the fluid solver, a rigid NACA0012 airfoil oscillating with a constant amplitude of $h_a = 0.175$ is chosen. Computations are carried out for the Reynolds numbers of 10,000 and 20,000 and for the Strouhal number (Str) of $0 < Str < 0.6$, which are defined as follows:

$$Re = \frac{U_0 c}{\nu}, \qquad Str = \frac{fc}{U_0} \tag{16}$$

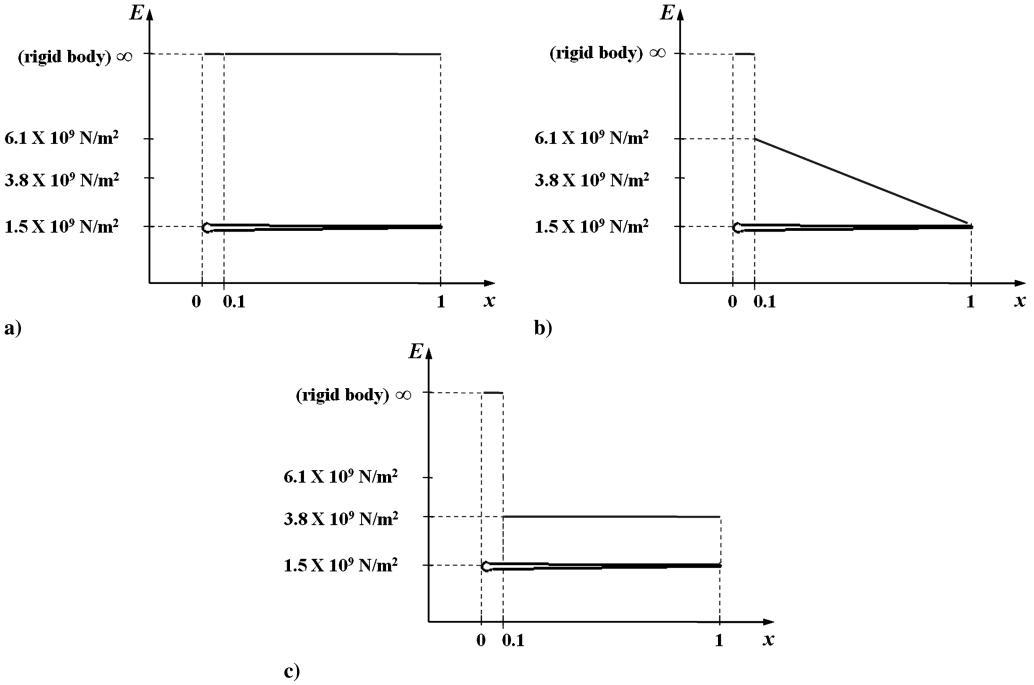

Fig. 4 Structural modeling: a) rigid airfoil, b) linear-type airfoil, and c) homogeneous -type airfoil.

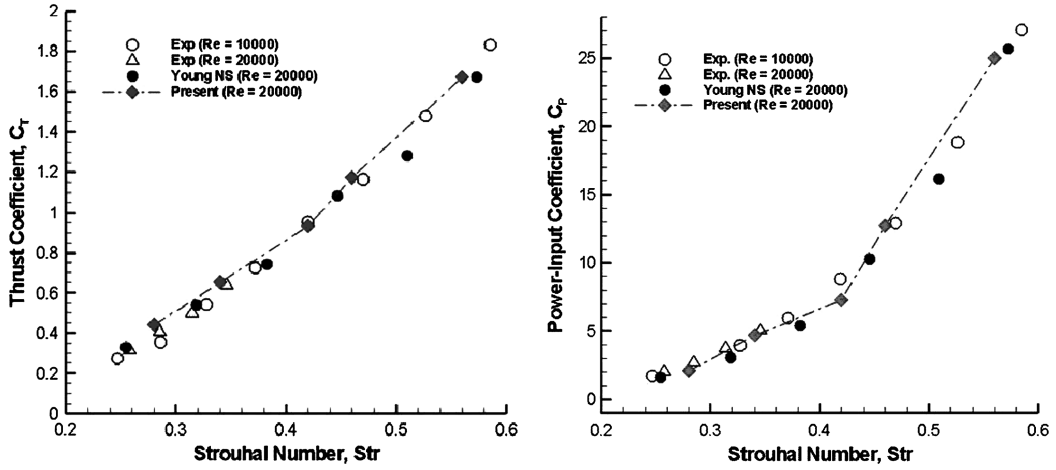

a) b)

Fig. 5 Comparison of numerical results with experimental data: a) thrust coefficient and b) power-input coefficient.

where U_0 is the incoming velocity, c is the chord length, ν is the kinematic viscosity, and f is the plunging frequency. The stroke of the plunging motion in each cycle is given by a sinusoidal function:

$$h(t) = h_a \cos(2\pi Strt) \tag{17}$$

where h_a is the dimensionless plunging amplitude normalized by the chord length c, and t is the dimensionless time.

The computed thrust and power-input coefficients are plotted as functions of the Strouhal number in Fig. 5. The thrust coefficient is given by

$$C_t = \frac{T}{\frac{1}{2}\rho U_0^2 c} \tag{18}$$

where T is the time-averaged thrust per unit span. The power-input coefficient is given by

$$C_p = \frac{F_y v}{\frac{1}{2}\rho U_0^3 c} \tag{19}$$

where $F_y v$ is the time-averaged instantaneous power input. The computed results are compared with the solutions obtained by Young and Lai [27] and to the results of an experiment on sinusoidal flapping airfoils conducted by Heathcote and Gursul [8]. Figure 5 shows that the present thrust and power-input coefficients are in very close agreement with experimental and other numerical results.

As a case for validating the solid module, a thick cylinder that is subjected to an internal pressure load is computed. The detailed contents can be found in [28]. The dimensional parameters of the test case are

$$a = 0.2 \text{ m}, \qquad b = 0.1 \text{ m}, \qquad P = 1.0 \times 10^8 \text{ Pa},$$
$$E = 2.1 \times 10^{11} \text{ Pa}, \qquad \rho = 7850 \text{ kg/m}^3, \quad \text{and} \quad \nu = 0.3$$

where a is the outer radius, b is the inner radius, P is the pressure load, E is the modulus of elasticity, ρ is the density, and ν is the Poisson ratio. Computation is performed with a number of 7288 triangular elements. Table 1 shows a comparison of the present results with the analytic solutions and numerical results obtained by the commercial code NISA. It is seen that the present inner and outer radial displacements are in very good agreement with other results within a relative error of 1%.

Table 1 Comparison of radial displacement

	Theoretical	NISA II	Present
Inner radial displacement	0.079365	0.079299	0.079944
Outer radial displacement	0.063492	0.063459	0.063784

B. Validation of FSI Solver

The present FSI solver is validated with the case of a flexible airfoil oscillating with a constant amplitude of $h_a = 0.175$. A water-tunnel experiment was performed by Heathcote and Gursul [8]. The airfoil is a 90 mm chord of teardrop/plate design, as shown in Fig. 6. The plate is a sheet of uniform thickness with a modulus of elasticity 2.05×10^{11} N/m^2, Poisson ratio 0.3, density 7850 kg/m^3, and length 60 mm. The teardrop element is of chord length 30 mm and made of solid aluminum. Two plates are considered with $b/c = 0.56 \times 10^3$ and 4.23×10^3, where b is the plate thickness and c is the chord length. Simulations are carried out for the Reynolds numbers

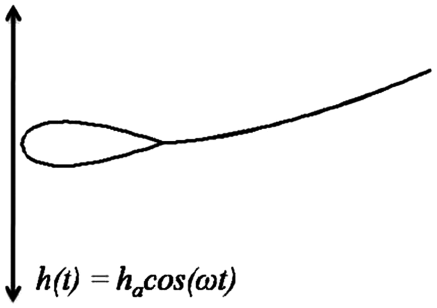

Fig. 6 Flat plate with a teardrop element at leading edge.

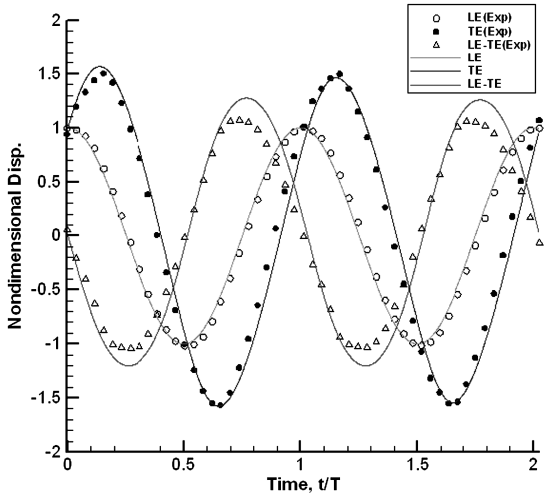

Fig. 7 Histories of displacements at leading and trailing edges ($Re = 9000$, $Str = 0.34$, $b/c = 0.56 \times 10^3$).

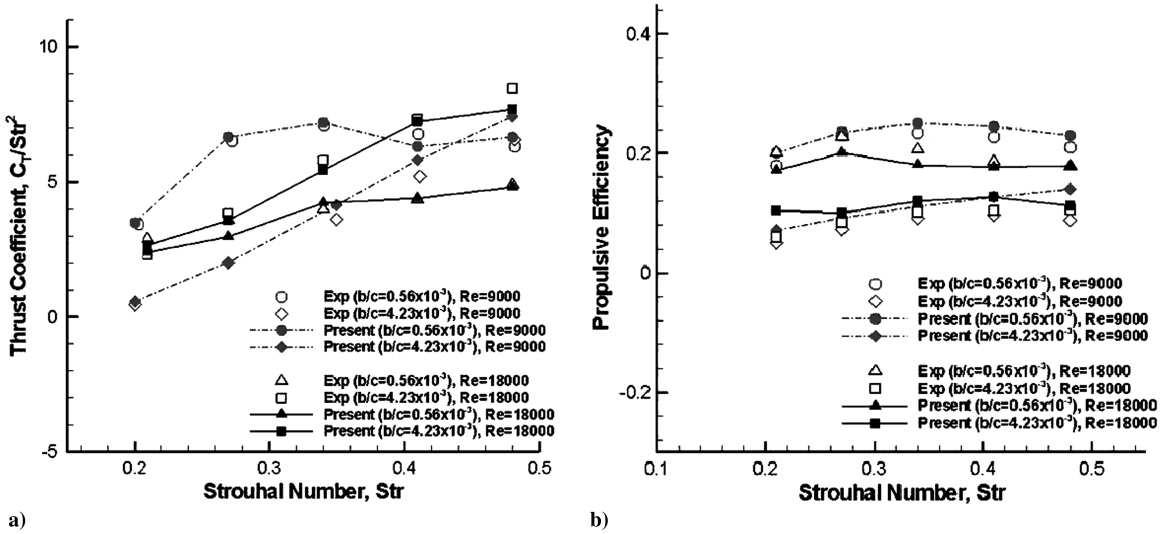

Fig. 8 Comparison of numerical results with experimental data: a) thrust coefficient and b) propulsive efficiency.

of 9000 and 18,000 and for the Strouhal number of $0.2 < Str < 0.5$. The motion of the airfoil is the same as in Eq. (17).

For the given Reynolds and Strouhal numbers, the computed temporal trajectories of the leading edge, trailing edge (the end point of the plate), and their relative distances are compared with the corresponding experimental measurements as in Fig. 7. It is clear that the present computations agree very well with experiments. Plots of the thrust coefficient and the propulsive efficiency in terms of the Strouhal number are also shown in Fig. 8 for two plate thicknesses. To facilitate graphical comparisons with various cases over the range of the Strouhal number considered, the thrust coefficients shown are divided by the square of the corresponding Strouhal numbers. The propulsive efficiency is defined by

$$\eta = \frac{TU_0}{F_y v} = \frac{C_t}{C_p} \tag{20}$$

From Fig. 8, close agreements are observed between the present computed results and the experimental measurements both for the thrust coefficient and the propulsive efficiency. Computations and experiments indicates that the thrust coefficient for $b/c = 4.23 \times 10^3$ increases more rapidly than for $b/c = 0.56 \times 10^3$ as the Strouhal number increases. On the other hand, the propulsive efficiency for $b/c = 0.56 \times 10^3$ is higher than for $b/c = 4.23 \times 10^3$ for all Strouhal numbers.

IV. Numerical Results

Qualitative comparisons of aerodynamic characteristics are first presented between rigid and flexible airfoils. Furthermore, three airfoils reflecting structural flexibility of a blowfly are used and their results are compared quantitatively. FSI flowfields are then examined by changing aerodynamic parameters, such as the Reynolds number and reduced frequency, to confirm that key physical phenomena can be observed in other flow conditions.

Table 2 Flapping-motion data from Nachtigall [13]

Parameter	Value
Airspeed U_0	2.75 m/s
Maximum relative speed $U_{\max}$	9.963 m/s
Chord length c	3.8 mm
Reynolds number Re_c	2523.92
Rotation center	10% of chord
Flapping frequency f	130.6 Hz
Reduced frequency k	0.049813

There are several ways to define the Reynolds number of an insect's flapping motion. Sometimes, the conventional way of defining the Reynolds number for fixed-wing aircraft may not be appropriate. For example, the Reynolds number based on the freestream velocity cannot be defined in the case of hovering because the conditions of airflow around the wings rapidly change throughout the whole wing beat cycle [23]. The Reynolds number in the present work is defined by using the maximum relative velocity of wing motion. All of the computed aerodynamic coefficients are also normalized by the maximum relative speed. Here, the maximum relative speed is the sum of the freestream velocity and the maximum wing velocity during the flapping motion. The flow conditions including nondimensional numbers are obtained from Nachtigall's [13] experimental data, as shown in Table 2.

An O-type grid of 289×113 with a wall spacing of 1×10^{-4} chord is used, and the outer boundary of the computational domain extends to 25 chords. An unstructured mesh of 244 cells is used for the solid domain. All computations are carried out for 10 cycles to obtain sufficiently periodic behavior of the aerodynamic coefficients. The fluid–structure coupling procedure at each time step proceeds as follows.

1) Receive the new airfoil shape from the solid module using the grid deformation method. (The initial airfoil shape is used in the first iteration.)

2) Obtain the flowfield information based on the updated airfoil shape.

3) Transfer the aerodynamic load to the solid module using the data method.

4) Obtain the airfoil deformation from the solid module, and transfer the displacement to the fluid module.

In this case, the physical time step of the fluid module is much larger than that of the solid module because the solid module is explicit and the allowable time step is directly proportional to the element size. The physical time steps between the two modules are synchronized with the loosely coupled FSI approach. For the given fluid time step, the solid module is advanced in multiple steps by the time step determined by Eq. (10). A time-step sensitivity analysis is carried out with three different levels of the fluid time step ($1/500T$, $1/1000T$, and $1/1500T$, where T is the nondimensional flapping period). For each fluid time step, the solid time step is fixed and the behavior of aerodynamic force generation is examined. As shown in Fig. 9, each result is almost the same. Based on this result, the physical time step of $1/1000T$ is chosen in the present computations.

A. Qualitative Comparison of Aerodynamic Characteristics

Figures 10 and 11 show histories of the instantaneous lift and thrust coefficients. Downstroke and upstroke are indicated by gray and white regions, respectively. Plots are shown for the rigid airfoil

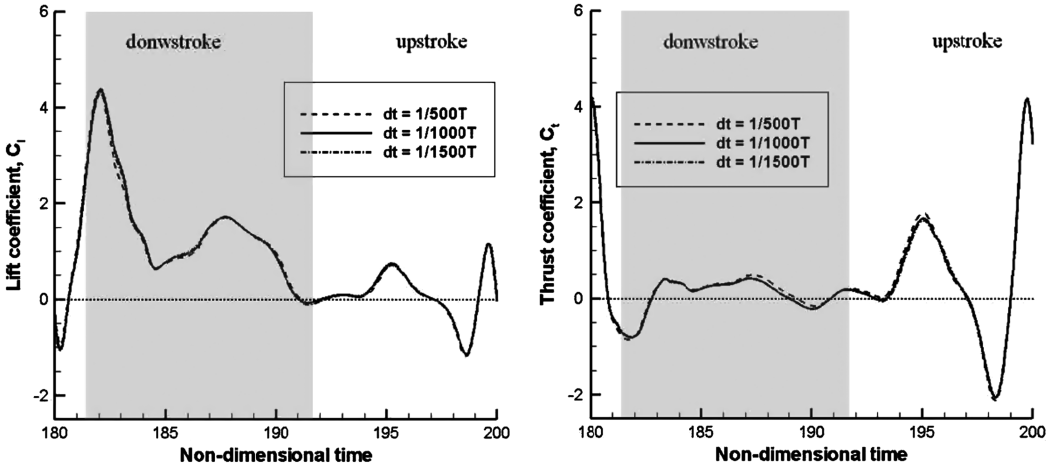

Fig. 9 Effect of time-step sensitivity on aerodynamic force generation: a) lift coefficient and b) thrust coefficient.

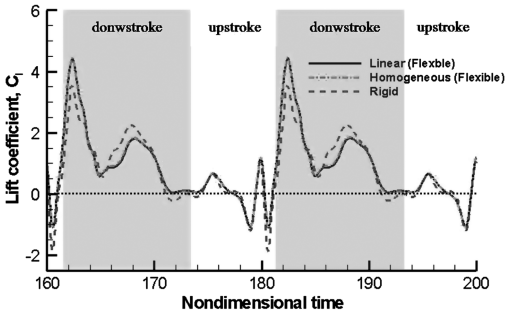

Fig. 10 Histories of instantaneous lift coefficients.

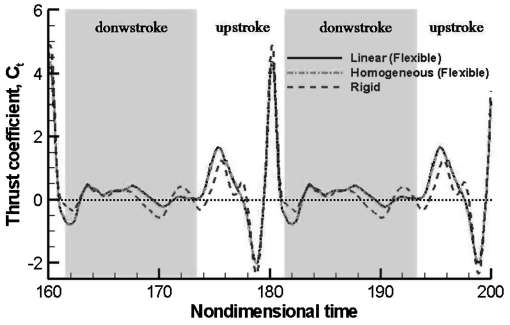

Fig. 11 Histories of instantaneous thrust coefficients.

and for linear and homogeneous types of flexible airfoils. In all three cases, Lift is mainly generated during downstroke motion, while thrust is impulsively produced at the end of upstroke. These results are similar to earlier findings from simulations of two-dimensional rigid elliptic airfoils [7].

Since the computed results of the two flexible airfoils are very similar, only the linear flexible airfoil is compared with the rigid airfoil. Figure 12 shows snapshots of the flow patterns around the two airfoils illustrating the formation and shedding of vortices at leading and trailing edges during downstroke. Figure 13 shows the sequential vorticity contours at the end of upstroke. Key physical phenomena and flow patterns such as the LEV, vortex pairing, and vortex staying are still observed in the flexible airfoil. Figure 14 depicts a comparison of pressure and velocity fields between the two airfoils at the beginning of downstroke. The center of the leading-edge vortex (LEV) and pressure suction is almost the same with each other. As a close-up view of Fig. 12a, Fig. 15 shows velocity and vorticity fields around the two airfoils in the wake region. A pair of vortices and a subsequent strong jet is clearly observed in both cases. Figure 16 shows the pressure and velocity distributions over the airfoils around $t = 180.254$ when thrust becomes maximal. The vortex-staying mechanism observed in both airfoils is almost the same.

At the same time, some differences are also observed as shown in Figs. 10. Early in downstroke, the flexible airfoil generates more lift. This is because the structural deformation induces a camber effect to the airfoil, which increases an effective angle of attack, as shown in Fig. 17. As a result, the size and intensity of the LEV is increased [2]. It is well known that the lift enhancement arises from the

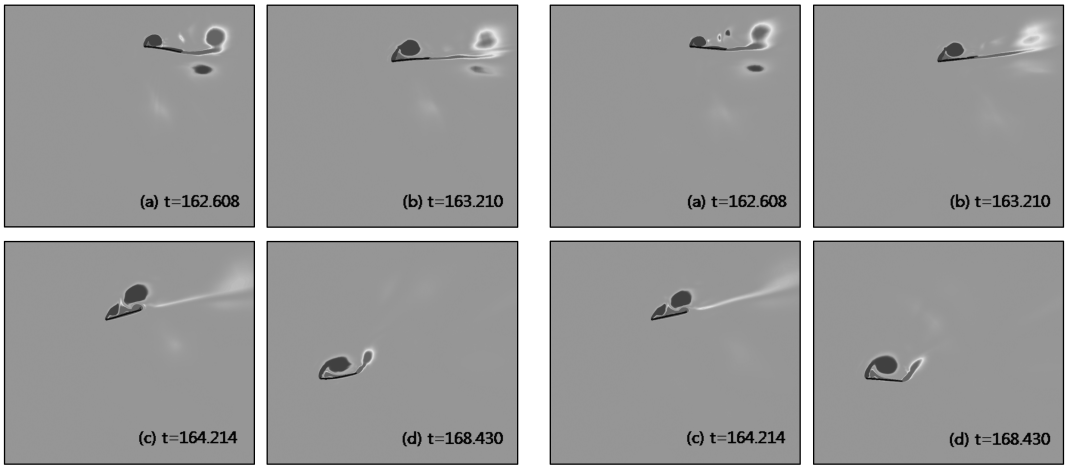

Fig. 12 Vorticity contours during downstroke: a) $t = 162.608$, b) $t = 163.210$, c) $t = 164.214$, and d) $t = 168.430$.

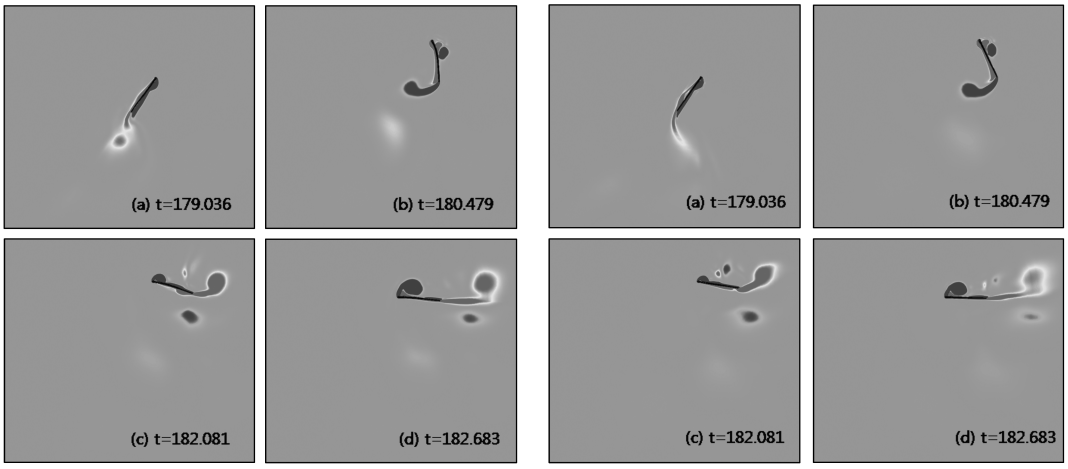

flexible airfoil **rigid airfoil**

Fig. 13 Vorticity contours during upstroke: a) $t = 179.036$, b) $t = 180.479$, c) $t = 182.081$, and d) $t = 182.683$.

development and shedding of the LEV. As shown in Fig. 18a, the low-pressure region at leading edge of the flexible airfoil is found to be wider and stronger than that of the rigid one. Figure 19 illustrates the magnitude and direction of the net force vector by integrating surface pressure (the effect of shear stress is negligible). In Fig. 19a, which corresponds to Fig. 18a, the magnitude of the net force vector is larger in the flexible airfoil because of higher pressure difference, and it eventually brings the lift enhancement in the flexible airfoil.

On the contrary, at the middle of downstroke, the rigid airfoil produces more lift than the flexible one. The flexible airfoil creates a negative camber effect due to structural flexibility, and now the effective angle of attack decreases (see Fig. 17). As a result, the vortex intensity at the middle of the upper surface is considerably weakened. This is clearly seen from Fig. 18b. When airfoil experiences structural deformation as in Fig. 19b, which corresponds to Fig. 18b, the net force vector acting on the airfoil is tilted forward, and lift component decreases accordingly. The tilting of the net force vector acts negatively by creating a thrust component.

At the end of downstroke, airfoil rotates clockwise and a counterclockwise rotating vortex sheds from the shear layer at trailing

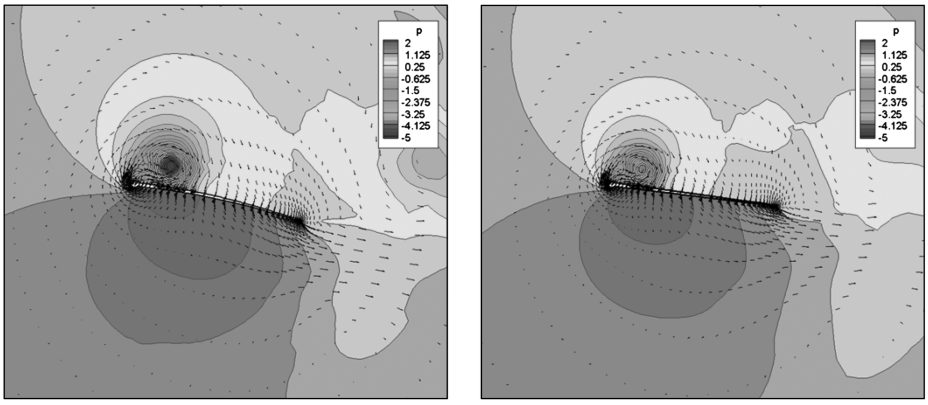

flexible airfoil **rigid airfoil**

Fig. 14 Leading-edge vortex at $t = 162.608$.

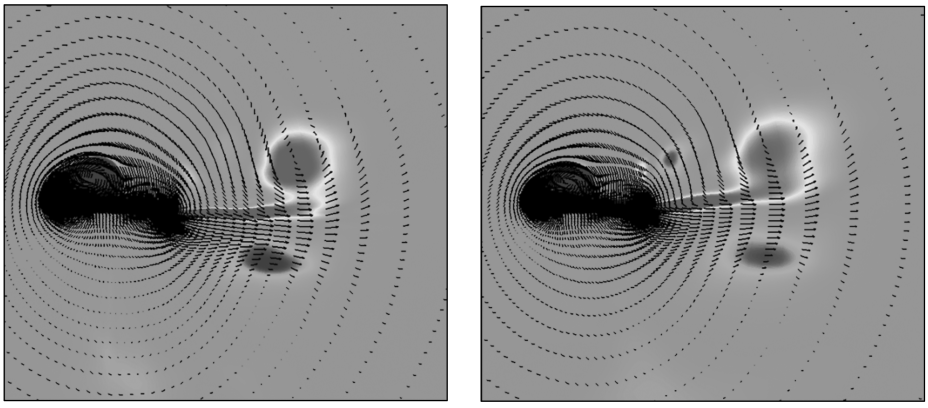

flexible airfoil **rigid airfoil**

Fig. 15 Vortex pairing and a jet flow in the wake at $t = 162.608$.

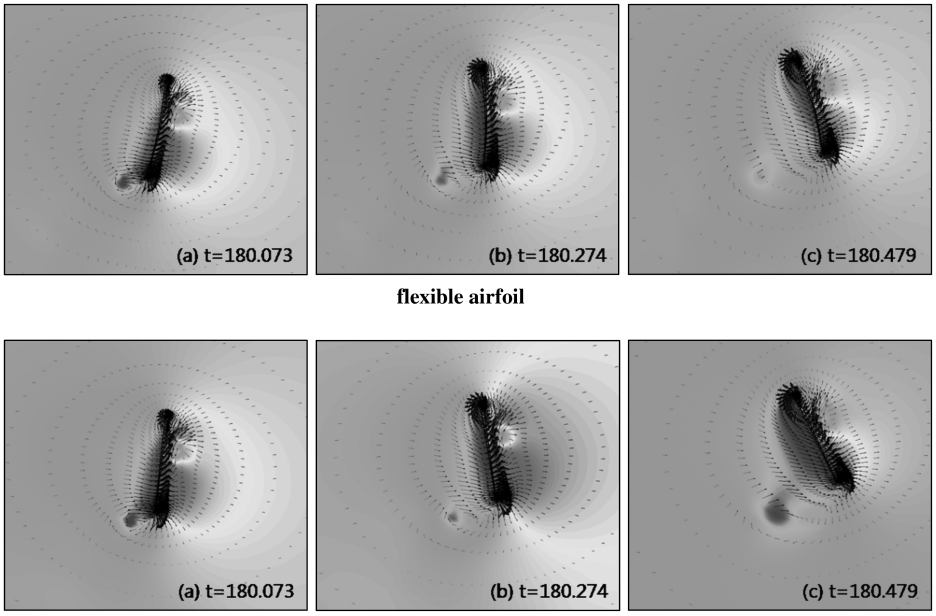

Fig. 16 Vortex staying: a) $t = 180.073$, b) $t = 180.274$, and c) $t = 180.479$.

edge (Fig. 18c). In case of the rigid airfoil, the vortex sheds earlier and stays away from trailing edge, and its intensity is somewhat weak. From the net force vector force in Fig. 19c (Fig. 18c), negative lift is produced. On the other hand, the vortex shedding from the flexible airfoil is stronger and it stays near trailing edge due to structural deformation. The low-pressure region at trailing edge produces a substantial pressure reversal, and the net pressure difference is close to zero. Consequently, the flexible airfoil generates a close-to-zero lift.

At the end of upstroke, the flexible airfoil is deformed due to the impulsive rotation, which weakens the intensity of the small-size LEV at the lower surface of leading edge (Fig. 18g). The intensity of the vortex is slightly stronger in the rigid airfoil, and a relatively lower pressure region is developed. In addition, the structural deformation changes the direction of the net force vector upward, as shown in Fig. 19d (Fig. 18g). Thus, the rigid airfoil produces a larger negative lift.

As shown in Fig. 11, the two airfoils also exhibit some differences in thrust generation. Early in downstroke, a higher negative thrust is observed in the flexile airfoil, which is caused by the camber effect (Fig. 18h). The camber effect increases the effective angle of attack, as shown in Fig. 17. A stronger pressure suction on the upper surface and a weaker vortex on the lower surface increases the net pressure difference, which acts positively in lift generation, but not in thrust generation.

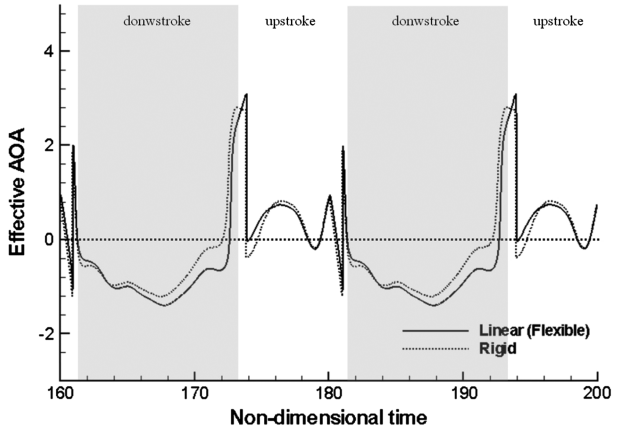

Fig. 17 Histories of effective angle of attack.

At the middle of downstroke, the flexible airfoil produces a higher thrust by the tilting of the net force vector (Figs. 18b and 19b). Geometric deformation induces a substantial tilting of the net force vector in the forward direction, and more thrust is generated in the flexible airfoil. In Fig. 18c, when the airfoil starts clockwise rotation at the end of downstroke, the flexible airfoil becomes a concave structure. As explained in lift generation, the rigid airfoil generates the downward net force, but the net force in the flexible airfoil becomes close to zero (Fig. 19c).

Also note that the direction of the net force vector is not perpendicular to the instantaneous total relative velocity, indicating that a simple Kutta–Joukowski theorem does not hold in this case due to the unsteady viscous effects at high effective angle of attack.

Early in upstroke, in Fig. 18d, a low-pressure region is widely developed at the lower surface of the flexible airfoil. This is due to the creation of the LEV, as shown in Fig. 20a. Unlike the rigid airfoil whose motion is almost parallel to the upstroke trajectory, the flexible airfoil has a nonzero angle of attack in the tangential direction of motion, and a small-size LEV is created. A region of relatively low pressure is formed, especially at the lower leading edge of the flexible airfoil, which produces more thrust component.

At the middle of upstroke, a thrust reversal can be observed between the two airfoils. The location of the LEV generated during downstroke is different, as shown in Figs. 18e and 20b. In the rigid airfoil, it is located at the middle of the upper surface, whereas it stays near the lower surface of the leading edge in the flexible airfoil. Thus, the net pressure difference is higher in the flexible airfoil, which results in a higher thrust. However, this situation is quickly reversed. From Figs. 18f, a new LEV is developed in the lower surface of the rigid airfoil, but not in the flexible airfoil. This is because a negative camber effect produced by the flexible airfoil decreases an effective angle of attack (see Fig. 17). Consequently, the net pressure difference becomes higher in the rigid airfoil (Fig. 18f) and thrust-generation pattern is reversed.

The strong jet yielding the thrust peak at the end of upstroke arises from the interaction of two counter-rotating vortices, and this vortex pairing mechanism is impulsively developed [7]. The vortex-staying mechanism caused by the impulsive rotation at the end of upstroke also gives rise to the pressure difference across the airfoil. As a consequence, the maximum thrust peak is generated. As in Figs. 11, 15, and 16, these phenomena are observed in the flexible as well as rigid airfoils.

In summary, key physical phenomena and flow patterns such as the LEV, vortex pairing, and vortex staying are essentially the same

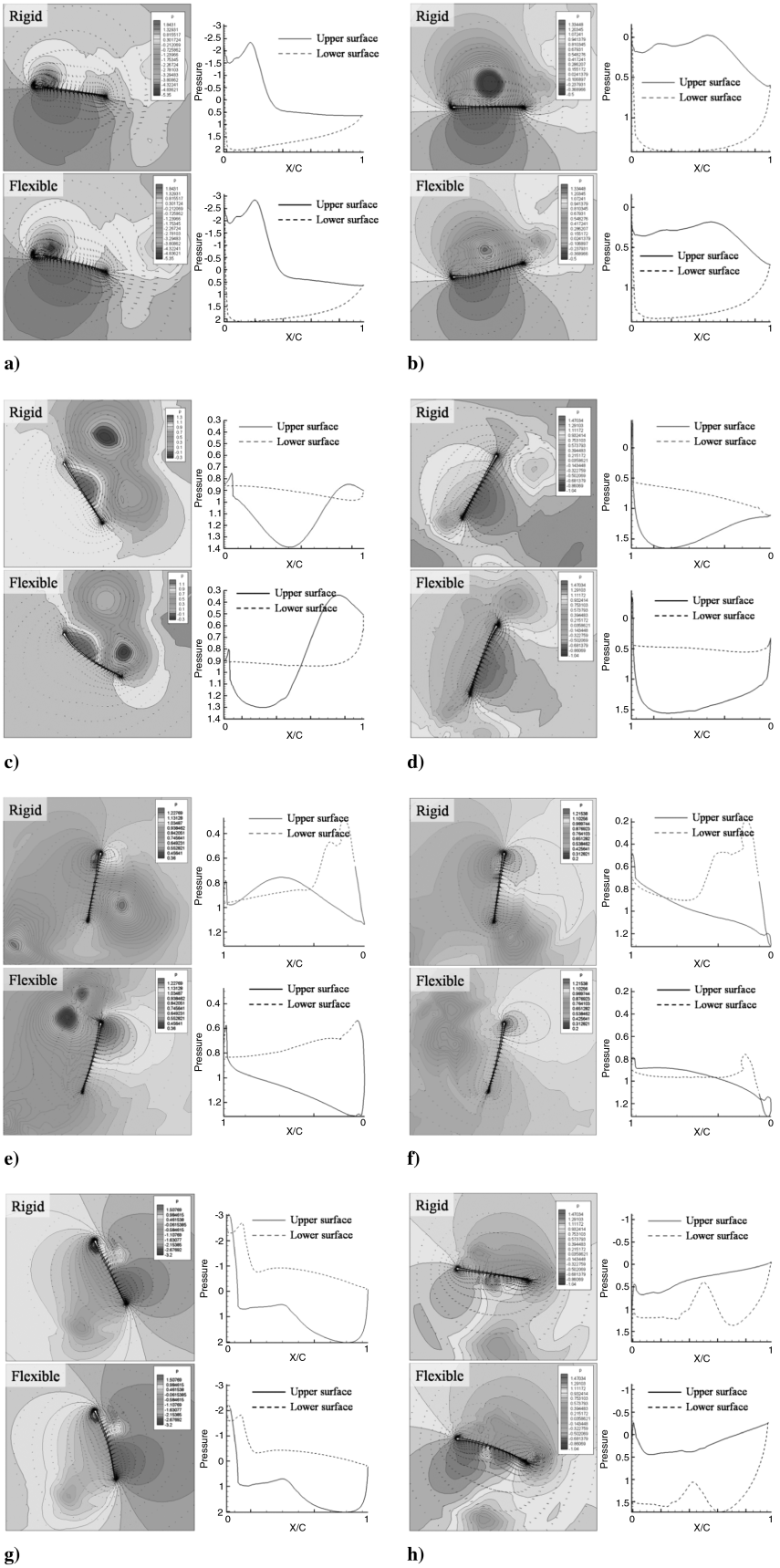

Fig. 18 Pressure and velocity fields (left), pressure distribution on the wall (right): a) $t = 162.608$, b) $t = 168.028$, c) $t = 171.642$, d) $t = 175.456$, e) $t = 176.660$, f) $t = 177.464$, g) $t = 180.475$, and h) $t = 181.604$.

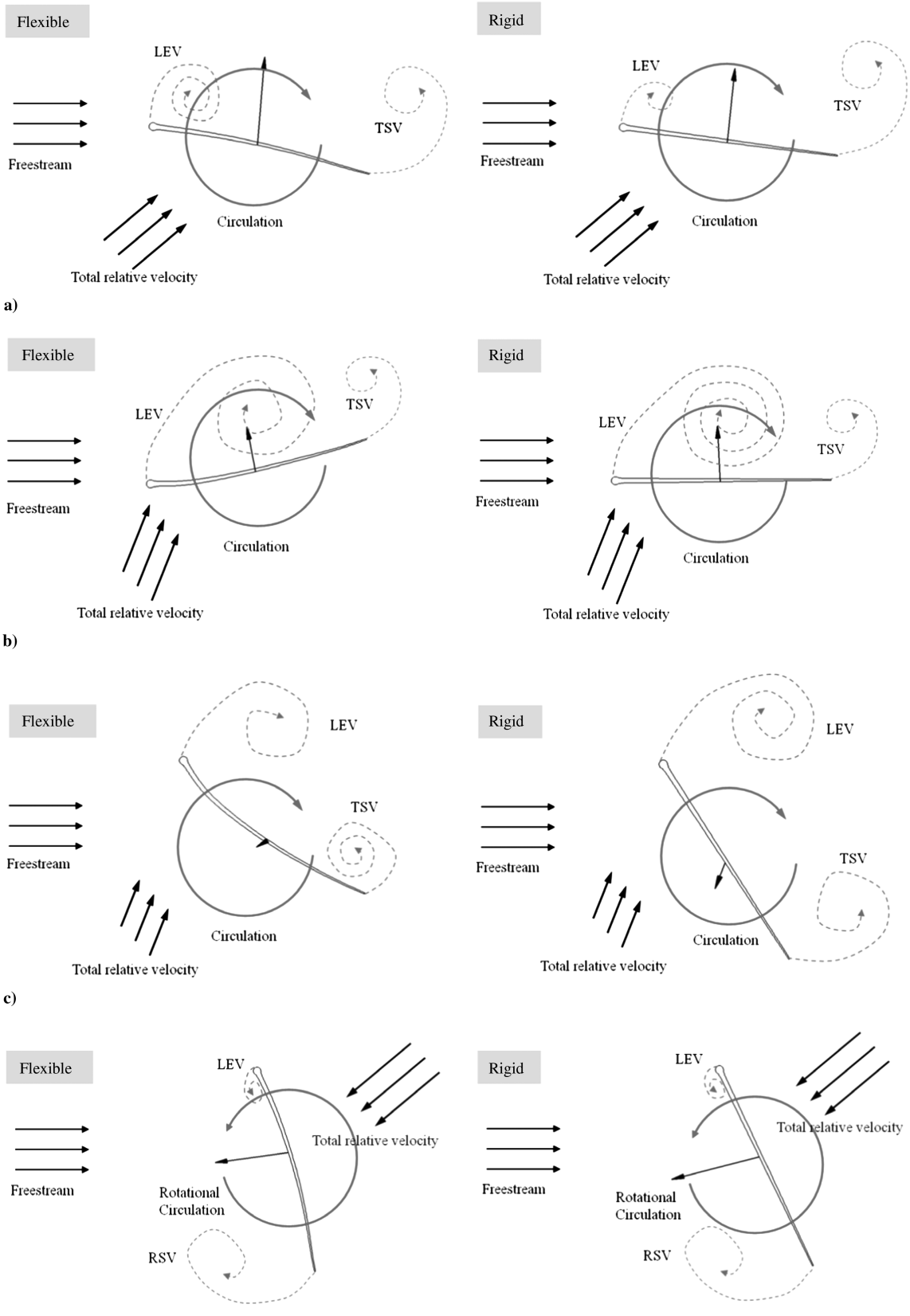

Fig. 19 Schematic summary of net force generation: a) $t = 162.608$, b) $t = 168.028$, c) $t = 171.642$, and d) $t = 180.475$.

even when structural flexibility is included. However, noticeable differences are also observed in lift and thrust generation, and they can be explained by the camber effect, vortex intensity, and tilting of the net force vector caused by structural deformation.

B. Quantitative Comparison on Aerodynamic Performance

Figures 10 and 11 show histories of the instantaneous lift and thrust coefficients of three airfoils. Overall characteristics are qualitatively similar, but quantitative results are somewhat different.

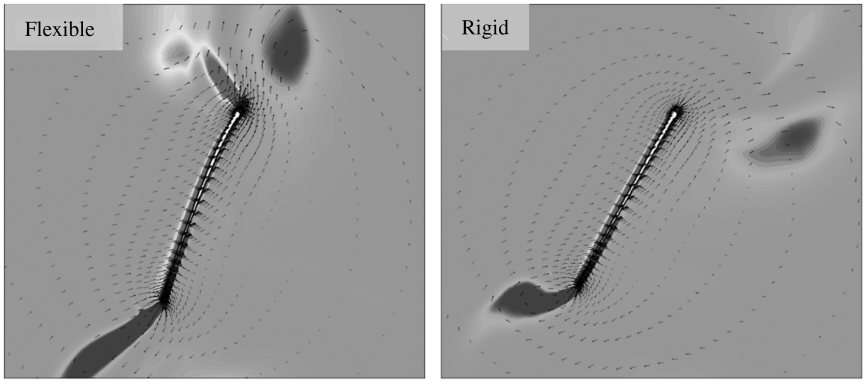

a)

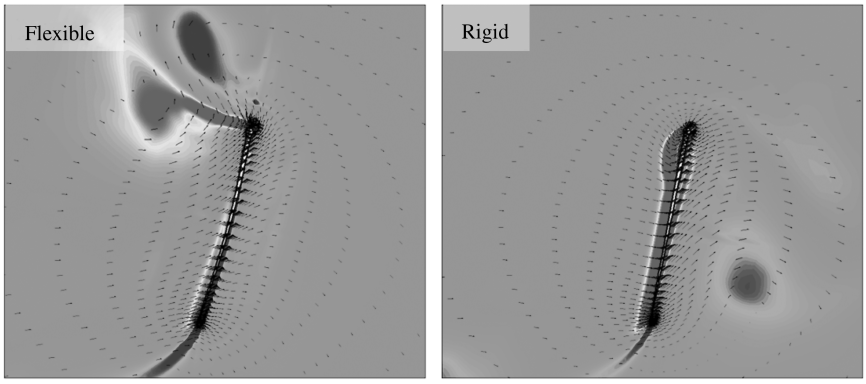

b)

Fig. 20 Vorticity contour and velocity fields: a) $t = 175.456$ and b) $t = 176.660$.

Table 3 compares the time-averaged mean lift and thrust coefficients and propulsive efficiency, which are evaluated by Eqs. (21) and (22):

$$\bar{c}_i = \frac{1}{T}\int_0^T c_i \, \mathrm{d}t \tag{21}$$

$$\eta = \frac{\bar{c}_T}{\bar{c}_P} \tag{22}$$

where c_i is the instantaneous aerodynamic coefficient, T is the period of one cycle, η is the propulsive efficiency, and the overbar denotes the mean value.

From Table 3, it is clear that flexible airfoils perform better than the rigid one in every respect. Compared with the rigid airfoil, the net lift is increased by about 12.8% in the homogeneous type. The net thrust and propulsive efficiency are enhanced by about 32.7% and 33.2% in the linear type.

Judging from the overall comparison, the linear-type flexible airfoil exhibits a most improved aerodynamic performance.

C. Effects of Aerodynamic Parameters

From the prior analysis, physical phenomena such as the LEV, vortex pairing, and vortex staying play a key role in generating sufficient aerodynamic forces. This has been observed in both the rigid and flexible airfoils. In this section, it is examined whether similar phenomena could be observed in other flight conditions. Generally, the frequency range of insect flapping is about 5–300 Hz, and the range of Reynolds number is $\mathcal{O}(10^2)$–$\mathcal{O}(10^4)$ [29,30]. Parametric study has been carried out by changing the Reynolds number and reduced frequency in the range of the flight conditions mentioned.

Table 3 Comparison of aerodynamic coefficients

	Rigid	Linear	Homogeneous
c_l	0.754	0.851	0.852
c_t	0.205	0.272	0.260
η	0.491	0.654	0.621

Considering the blowfly's flight condition, FSI simulations are carried out for the Reynolds numbers ranging from 500 to 4,500 and the reduced frequency ranging from 0.04 to 0.09 (frequency range of about 20–235 Hz). In all simulations, the wing trajectory keeps the same and the linear-type airfoil is used.

Figures 21 and 22 show histories of the lift and thrust coefficients for various flight conditions. Each figure shows the behavior of force coefficients depending on the change of the Reynolds number at a given reduced frequency. When the reduced frequency is greater than 0.06, the range of the Reynolds number is limited up to 2523.92. This is because the Reynolds number and reduced frequency are both determined by the realizable flight condition, i.e., the maximum relative speed. If the Reynolds number exceeds 2523.92 with a given reduced frequency (0.06–0.09 in Figs. 21 and 22), the maximum relative speed yields too much deformation, which cannot be observed in real flight condition. In low reduced frequency (0.04 and 0.049813 in Figs. 21 and 22), a high-Reynolds-number condition is still realizable. From Figs. 21 and 22, overall pattern for lift and thrust generation is qualitatively quite similar, but at the same time, some quantitative differences are also visible. Figure 23 shows snapshots of the vortex pairing for various conditions. Depending on the reduced frequency, the intensity of the two vortices (or the strength of the induced jet) is different, but all cases clearly show that the two counter-rotating vortices are vertically aligned to produce a strong jet. The LEV and vortex staying can be observed in all cases, as shown in Figs. 24 and 25. As in Fig. 23, the vortex strength increases as the reduced frequency.

By changing aerodynamic parameters in other realizable flight conditions, it is confirmed that key physical phenomena such as the LEV and vortex pairing and vortex-staying mechanisms are observed

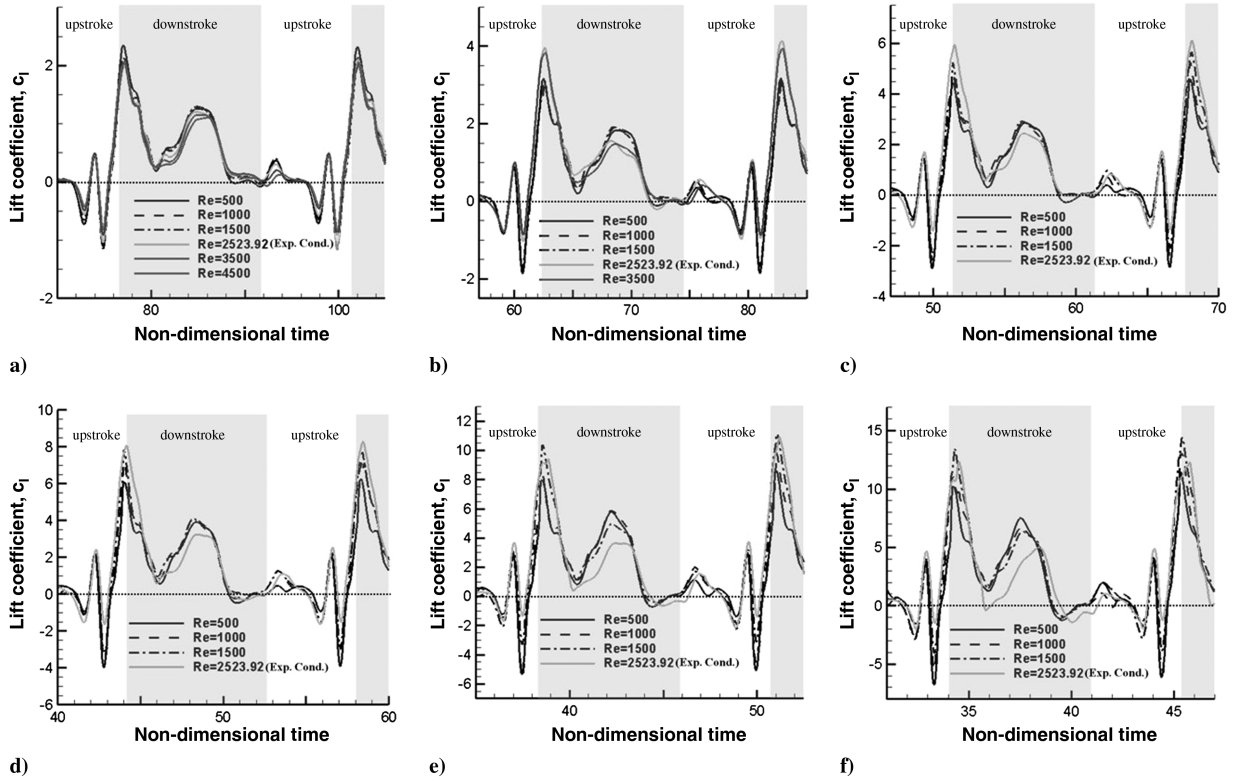

Fig. 21 Histories of lift coefficients under various flight conditions: a) $k = 0.04$, b) $k = 0.049813$ (experimental condition), c) $k = 0.06$, d) $k = 0.07$, e) $k = 0.08$, and f) $k = 0.09$.

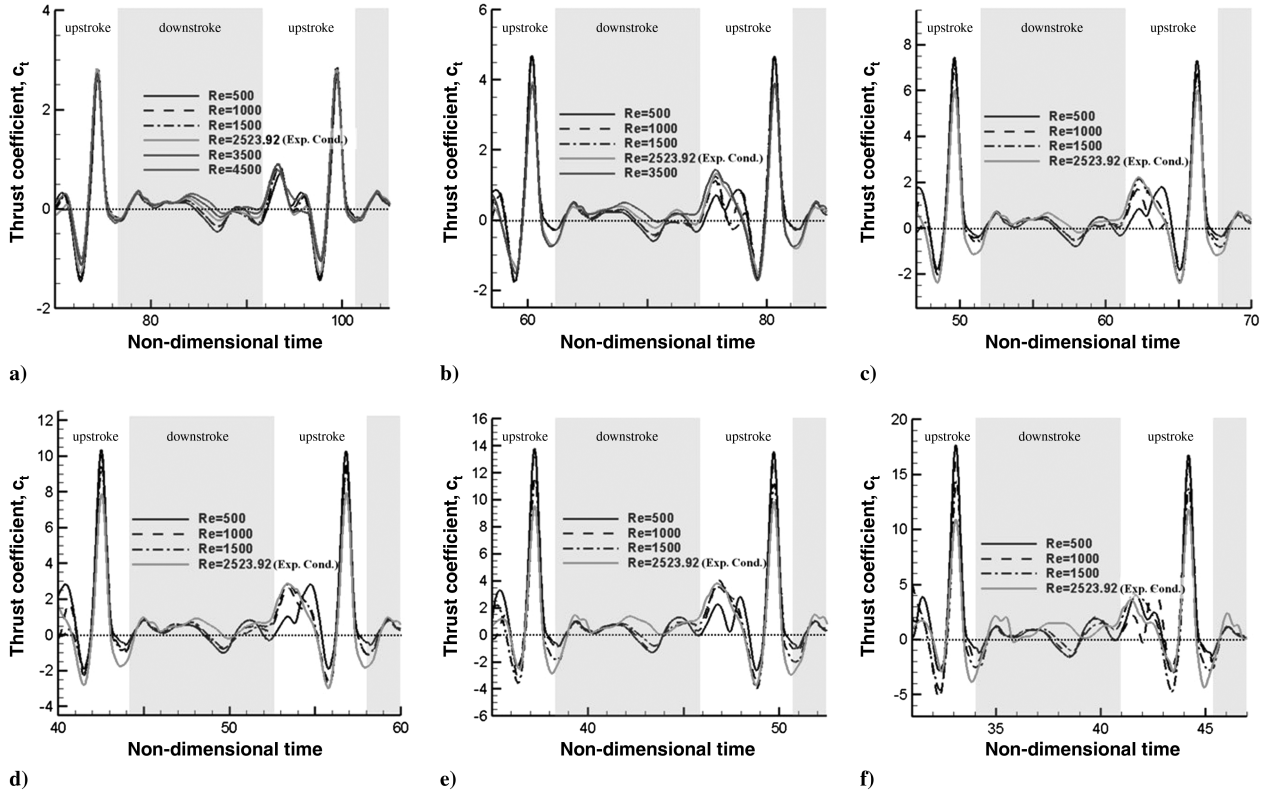

Fig. 22 Histories of thrust coefficients under various flight conditions: a) $k = 0.04$, b) $k = 0.049813$ (experimental condition), c) $k = 0.06$, d) $k = 0.07$, e) $k = 0.08$, and f) $k = 0.09$.

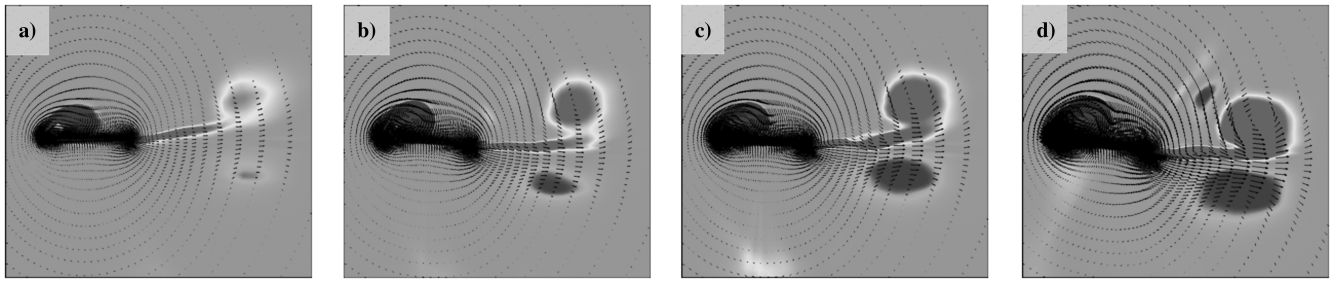

Fig. 23 Vortex pairing: a) $Re = 2523.92$, $k = 0.04$, b) $Re = 2523.92$, $k = 0.049813$ (experimental condition), c) $Re = 2523.92$, $k = 0.07$, and d) $Re = 2523.92$, $k = 0.09$.

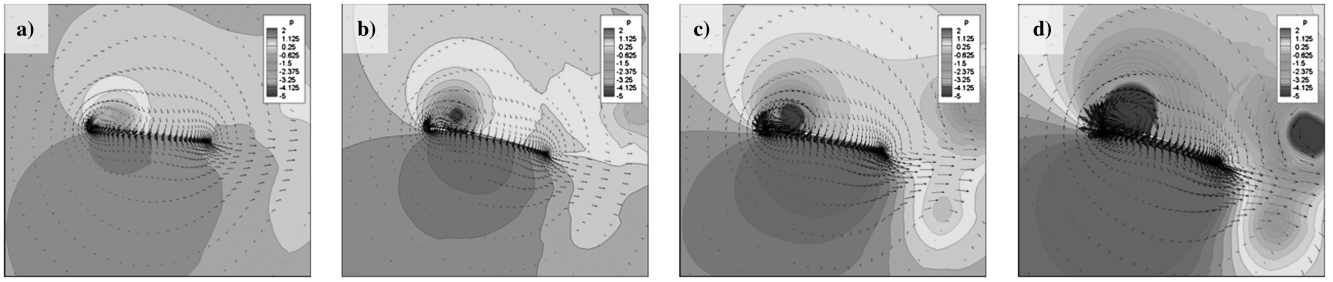

Fig. 24 Leading-edge vortex: a) $Re = 2523.92$, $k = 0.04$, b) $Re = 2523.92$, $k = 0.049813$ (experimental condition), c) $Re = 2523.92$, $k = 0.07$, and d) $Re = 2523.92$, $k = 0.09$.

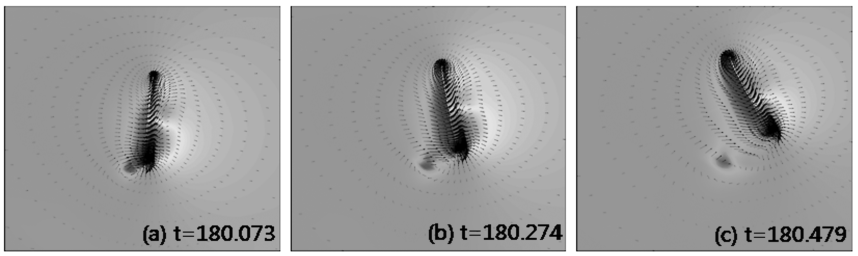

***Re* = 2523.92, *k* = 0.04**

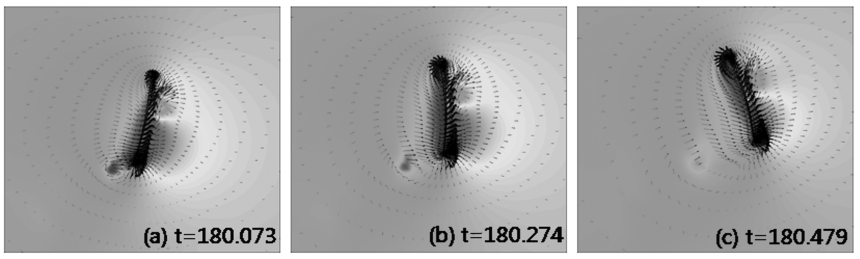

***Re* = 2523.92, *k* = 0.07**

Fig. 25 Vortex staying.

in all cases. This indicates that key physical phenomena provide important clues to understand the rapid maneuverability of insect flight in other flight conditions.

V. Conclusions

FSI simulations of unsteady viscous incompressible flows over an insectlike flexible airfoil are carried out to investigate the effects of wing flexibility under a forward-flight condition. FSI simulations have been conducted using the loose coupling method. The wing trajectory, geometric shape, and material properties are extracted from experimental data. Two flexible airfoils composed of the linear and homogeneous types are compared with the rigid airfoil under various flight conditions.

Through detailed comparisons of the rigid and flexible airfoils, it is seen that overall behavior of aerodynamic coefficients is qualitatively quite similar. However, structural deformation brings the changes of the effective angle of attack, the vortex intensity, and the tilting of the net force vector. As a result, quantitative differences are clearly visible. Comparisons of the computed aerodynamic coefficients reveal that the flexible airfoil does generate a higher performance. The net lift is improved by about 13% in the homogeneous flexible airfoil, while the net thrust and propulsive efficiency are enhanced by about 33% in the linear type. This indicates that wing flexibility is important in understanding or designing an insectlike flapping airfoil. From extensive FSI simulations, it is also confirmed that key flow characteristics such as the LEV, vortex pairing, and vortex staying can be observed in other forward-flight conditions.

Consequently, structural flexibility is essential in improving overall aerodynamic performance of flapping flight, and it can be beneficially exploited in the design of insectlike aerial vehicles.

Acknowledgments

The current work is supported by the Korea Science and Engineering Foundation (KOSEF) grant funded by the Korea government (MEST) (no. 20090084669). The authors appreciate the financial support provided by the National Space Laboratory program through the National Research Foundation of Korea that is funded by the Ministry of Education, Science, and Technology (grant 20090091724). This research is also supported by the Ministry of Land, Transport and Maritime Affairs through the Super Long Span Bridge Research and Development Center in Korea. The first author also appreciates the financial support provided by Hi Seoul Science/ Humanities Fellowship from Seoul Scholarship Foundation.

References

[1] Anderson, J. M., Streitlien, K., Barrett, D. S., and Triantafyllou, M. S., "Oscillating Foils of High Propulsive Efficiency," *Journal of Fluid Mechanics*, Vol. 360, No. 1, 1998, pp. 41–72. doi:10.1017/S0022112097008392

[2] Tuncer, I. H., and Platzer, M. F., "Computational Study of Flapping Airfoil Aerodynamics," *Journal of Aircraft*, Vol. 37, No. 3, 2000, pp. 514–520. doi:10.2514/2.2628

[3] Wang, Z. J., "Vortex Shedding and Frequency Selection in Flapping Flight," *Journal of Fluid Mechanics*, Vol. 410, 2000, pp. 323–341. doi:10.1017/S0022112099008071

[4] Lewin, G. C., and Haj-Hariri, H., "Modelling Thrust Generation of a Two-Dimensional Heaving Airfoil in a Viscous Flow," *Journal of Fluid Mechanics*, Vol. 492, 2003, pp. 339–362. doi:10.1017/S0022112003005743

[5] Lee, J. S., Kim, C., and Kim, K. H., "A Design of Flapping-Airfoil for Optimal Aerodynamic Performance in Low-Reynolds Number Flows," *AIAA Journal*, Vol. 44, No. 9, 2006, pp. 1960–1972. doi:10.2514/1.15981

[6] Kaya, M., and Tuncer, I. H., "Nonsinusoidal Path Optimization of a Flapping Airfoil," *AIAA Journal*, Vol. 45, No. 8, 2007, pp. 2075–2082. doi:10.2514/1.29478

[7] Lee, J. S., Kim, J. H., and Kim, C., "Numerical Study on the Unsteady-Force-Generation Mechanism of Insect Flapping Motion," *AIAA Journal*, Vol. 46, No. 7, 2008, pp. 1835–1848. doi:10.2514/1.35646

[8] Heathcote, S., and Gursul, I., "Flexible Flapping Airfoil Propulsion at Low Reynolds Numbers," *AIAA Journal*, Vol. 45, No. 5, 2007, pp. 1066–1079. doi:10.2514/1.25431

[9] Pederzani, J., and Haj-Hariri, H., "Numerical Analysis of Heaving Flexible Airfoils in a Viscous Flow," *AIAA Journal*, Vol. 44, No. 11, 2006, pp. 2773–2779. doi:10.2514/1.21203

[10] Olivier, M., Dumas, G., and Morissette, J. F., "A Fluid-Structure Interaction Solver for Nano-Air-Vehicle Flapping Wings," AIAA Paper 2009-3676, 2009.

[11] Chandar, D. D. J., and Damodaran, M., "Computational Fluid-Structure Interaction of a Flapping Wing in Free Flight Using Overlapping Grids," AIAA Paper 2009-3849, 2009.

[12] Shyy, W., Aono, H., Chimakurthi, S. K., Trizila, P., Kang, C.-K., Cesnik, C. E. S., and Liu, H., "Recent Progress in Flapping Wing Aerodynamics and Aeroelasticity," *Progress in Aerospace Sciences*, Vol. 46, No. 7, 2010, pp. 284–327. doi:10.1016/j.paerosci.2010.01.001

[13] Nachtigall, W., *Insects in Flight*, McGraw-Hill, New York, 1974.

[14] Guruwamy, G. P., "A New Modular Approach for Tightly Coupled Fluid/Structure Analysis," *International Journal of Aerospace Innovations*, Vol. 1, No. 1, 2009, pp. 1–10. doi:10.1260/175722509787549480

[15] Cerbral, J. R., and Lohner, R., "Conservative Load Projection and Tracking for Fluid-Structure Problems," *AIAA Journal*, Vol. 35, No. 4, 1997, pp. 687–692. doi:10.2514/2.158

[16] Rogers, S., and Kwak, D., "Upwind Differencing Scheme for the Time-Accurate Incompressible Navier– Stokes Equations," *AIAA Journal*, Vol. 28, No. 2, 1990, pp. 253–262. doi:10.2514/3.10382

[17] Cook, R. D., Malkus, D. S., Plesha, M. E., and Witt, R. J., *Concepts and Applications of Finite Element Analysis*, Wiley, New York, 2002.

[18] Jiao, X., and Heath, M. T., "Common-Refinement-Based Data Transfer Between Non-Matching Meshes in Multiphysics Simulations," *International Journal for Numerical Methods in Engineering*, Vol. 61, 2004, pp. 2402–2427. doi:10.1002/nme.1147

[19] Liu, X., Qin, N., and Xia, H., "Fast Dynamic Grid Deformation Based on Delaunay Graph Mapping," *Journal of Computational Physics*, Vol. 211, No. 2, 2006, pp. 405–423. doi:10.1016/j.jcp.2005.05.025

[20] Ok, H., "Development of an Incompressible Navier–Stokes Solver and Its Application to the Calculation of Separated Flows," Ph.D. Thesis, Univ. of Washington, Seattle, WA, 1993.

[21] Sane, S., "The Aerodynamics of Insect Flight," *Journal of Experimental Biology*, Vol. 206, No. 23, 2003, pp. 4191–4208. doi:10.1242/jeb.00663

[22] Wang, Z. J., "Dissecting Insect Flight," *Annual Review of Fluid Mechanics*, Vol. 37, 2005, pp. 183–210. doi:10.1146/annurev.fluid.36.050802.121940

[23] Brodsky, A. K., *The Evolution of Insect Flight*, Oxford Univ. Press., Oxford, 1994.

[24] Lee, J. S., "Numerical Study on Flapping-Airfoil Design and Unsteady Mechanism of Two-Dimensional Insect Wing," Ph.D. Thesis, Seoul National Univ., Seoul, ROK, 2006.

[25] Kesel, A., Philippi, U., and Nachtigall, W., " Biomechanical Aspects of the Insect Wing: An Analysis Using the Finite Element Method," *Computers in Biology and Medicine*, Vol. 28, No. 4, 1998, pp. 423–437. doi:10.1016/S0010-4825(98)00018-3

[26] Wainwritght, S., *Mechanical Design in Organisms*, Princeton Univ., Princeton, NJ, 1982.

[27] Young, J., and Lai, J., "Oscillation Frequency and Amplitude Effects on the Wake of a Plunging Airfoil," *AIAA Journal*, Vol. 42, No. 10, 2004, pp. 2042–2052. doi:10.2514/1.5070

[28] Young, C., *Roark's Formulas for Stress & Strain*, 6th ed., McGraw–Hill, New York, 1989.

[29] David, N., Stephen, L., and Hayward, G., "Relationship Between Wing Loading, Wingbeat, Frequency and Body Mass in Homopterous Insects," *Journal of Experimental Biology*, Vol. 135, 1998, pp. 9–23.

[30] Dudley, R., *The Biomechanics of Insect Flight*, Princeton Univ., Princeton, NJ, 2000.